Simultaneous Imaging and Spectroscopy of the Solar Atmosphere: Advantages and Challenges of a 3-Order Slitless Spectrograph

Charles C. Kankelborg[a] and Roger J. Thomas[b]

[a]Montana State University, Department of Physics,
Bozeman, MT 59717, USA
[b]NASA/Goddard Space Flight Center, Code 682,
Greenbelt, MD 20771, USA

ABSTRACT

The dynamic solar atmosphere poses a severe observational challenge for imaging spectroscopy in EUV. The traditional method of building up images by rastering a slit spectrograph has so far proven too slow to keep up with the Sun's rapidly changing transition region and corona. We describe a new approach, using a slitless imaging spectrograph operating in a narrow band, with imaging detectors at three orders. This arrangement offers cotemporal imaging and spectroscopy at high spatial, spectral, and temporal resolution. The prospect of disentangling spatial and spectral information is greatly improved by choosing a narrow band containing only two spectral lines, and by imaging at several spectral orders.

This paper discusses several advantages and challenges of the multi-order slitless approach. We derive a mathematical description of the "null space" of spatial-spectral signatures to which an ideal three-order slitless spectrograph has zero response. An exploration of the null space helps to clarify the capabilities and limitations of this instrument type. We infer that the three-order slitless spectrograph is sensitive to line intensity, doppler shift and line width; but insensitive to line asymmetry. Strategies are developed to minimize the ambiguity in interpreting the multi-order data.

A proof of concept sounding rocket payload, the *Multi-Order Solar EUV Spectrograph* (*MOSES*), is under development with an anticipated launch in Spring, 2004.

Keywords: Sun, chromosphere, corona, EUV, imaging, spectroscopy

1. INTRODUCTION

The solar corona and transition region emit radiation in many UV, EUV, and soft X-Ray emission lines. However, this hot, highly ionized, magnetized atmosphere evolves on timescales that are too fast for existing remote-sensing instruments. For example, the solar corona has a sound speed of ∼100 km/s and an Alfven speed of ∼1000 km/s. These are the relevant speeds for fundamental dynamical phenomena involving gas pressure gradients and magnetic stresses, respectively. The Transition Region and Coronal Explorer (TRACE)[1] observes in several EUV and FUV bands with resolution close to the limit of its 0.″5 (360 km) pixels, at the fastest cadence attained so far in EUV. The TRACE observations show complex features and rapid dynamics at all spatial scales.[2] At the TRACE resolution of 360 km per pixel, the timescales for dynamical phenomena are 0.4-3.6 s. With cadences of ∼5-50 s even the TRACE image sequences show considerable differences in detail between frames.

The time cadence difficulty we have just described is greatly compounded for slit spectrographs that must scan to build up a 2D image (§2). Nevertheless, the dynamical processes responsible for heating the corona, powering solar flares and triggering coronal mass ejections are likely to be elucidated only with combined imaging and

Further author information: (Send correspondence to C.C.K.)
C.C.K.: Email: kankel@icarus.physics.montana.edu, Telephone: 1 406 994 7853
R.J.T.: Email: thomas@jet.gsfc.nasa.gov, Telephone: 1 301 286 7921

UV/EUV and Visible Space Instrumentation for Astronomy and Solar Physics, Oswald H. W. Siegmund, Silvano Fineschi, Mark A. Gummin, Editors, Proceedings of SPIE Vol. 4498 (2001)

spectroscopy. Perhaps the best compromise to date has been to arrange co-observing between imaging and spectroscopic instruments. In many of the *SOHO* observing campaigns, imagers provide necessary context for the interpretation of spectroscopic data, while spectroscopic observations reveal the physics behind the images. The Solar-B instrument suite likewise combines imagers and a slit spectrograph.[3] The chief difficulty of this approach has been that the spectrograph slit is rarely in the right place at the right time. The ongoing efforts within the solar physics community to bring together imaging and spectroscopy in EUV testify to the scientific importance of this goal, and to the difficulty of accomplishing it.

Is there any hope of obtaining 2D maps of line ratios, doppler shifts, and other important spectroscopic parameters at a cadence that is comparable to dynamical timescales? We believe so.This paper describes the novel concept of a *narrowband, multi-order slitless spectrograph*, offering a unique combination of cotemporal imaging and spectroscopy at high cadence. A conceptual introduction to the technique is offered in §2. Several approaches to extracting spectroscopic information from the multi-order data are summarized in §3. §4 discusses some of the difficulties that will be encountered in data analysis, and some practical ways of reducing ambiguity in interpretation. In §5, we outline a proof-of-concept sounding rocket payload, the *Multi-Order Solar EUV Spectrograph* (*MOSES*), planned for launch in Spring, 2004.

2. OPERATING PRINCIPLE

The *narrowband multi-order slitless spectrograph* is a new type of instrument that delivers 2D imaging and spectroscopy at spatial and temporal resolution comparable to a pure imaging system.

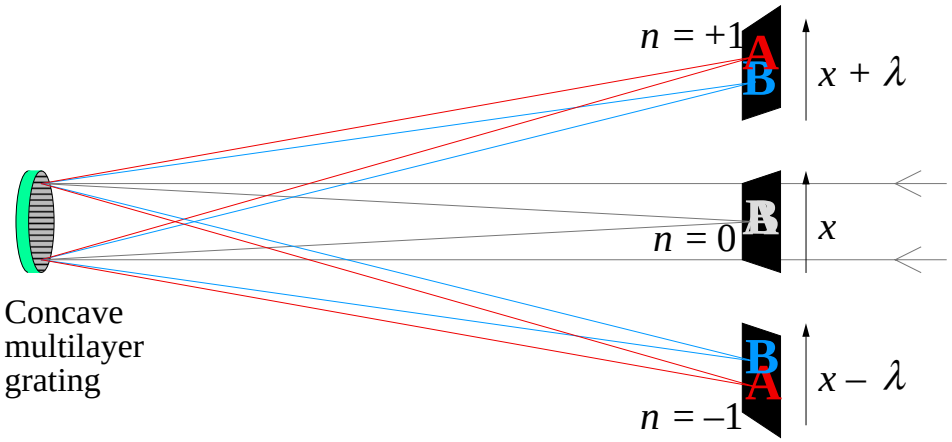

Figure 1. Sketch of a multi-order slitless spectrograph.

A slit spectrograph such as CDS[4] or SUMER[5] on *SOHO* builds up an image by scanning a slit across the field of view. Because it takes a long time to build up the field of view by rastering, the resulting "image" is not cotemporal; spatial and temporal information are entangled. Slow rastering makes it very difficult to study the evolution of dynamic solar features.

A slitless spectrograph such as *e.g.* Skylab S032A[6] achieves simultantaneous 2D imaging and spectra. As figure 3 shows, the 2-dimensional detector records intensity as a function of position mixed with wavelength: $I(x + \lambda, y)$. The disadvangage of this "overlappograph" method is the overlapping of spectral and spatial information in an extended source such as the sun.

We overcome the limitation of the slit spectrograph by placing detectors at several diffraction orders, $n = -1, 0, +1$. The formation of images at three orders is illustrated in figure 1. The figure indicates that an extended object, imaged in emission lines A and B in the instrument passband, will produce three unique images: one at each of the three spectral orders. These three images may be denoted $I_-(x - \lambda, y)$, $I_0(x, y)$ and $I_+(x + \lambda, y)$, where (x, y) are spatial coordinates in the object plane, and λ is wavelength. For convenience, each of these coordinates is measured in detector pixels.

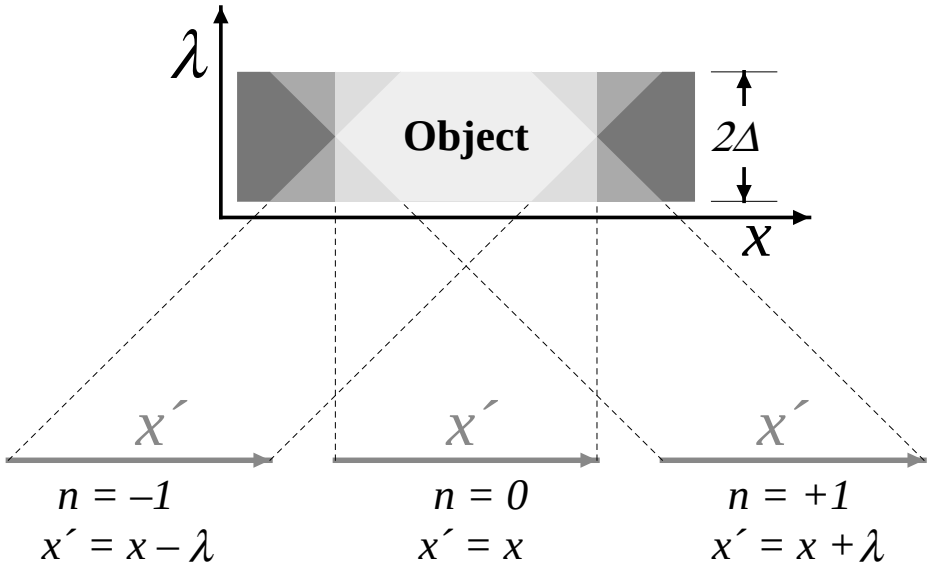

Figure 2. A multi-order slitless spectrograph images an object in (x, λ) space from several different "viewing angles".

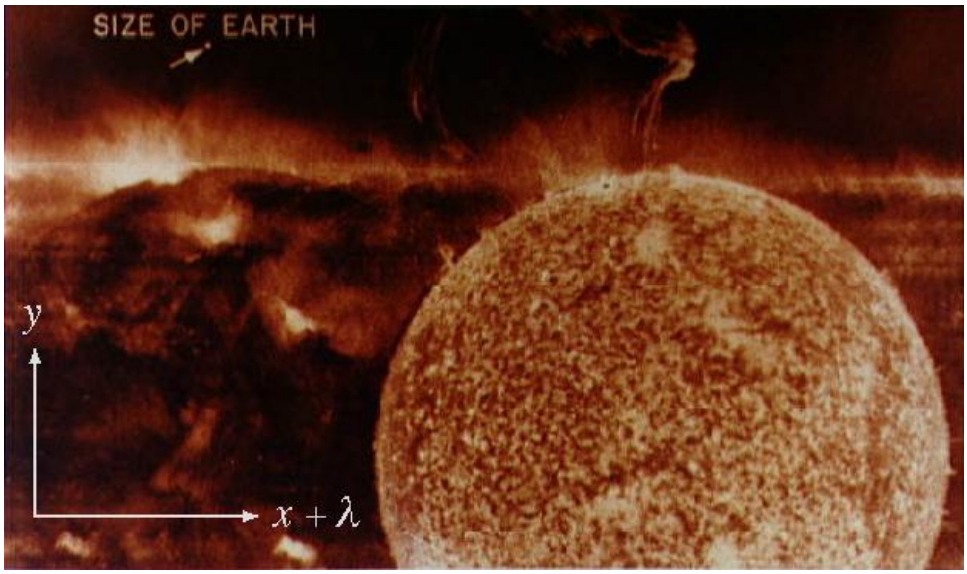

Figure 3. Part of an image from the Skylab S032A experiment. Detector coordinates corrspond to $(x + \lambda, y)$. A large filament eruption is shown in He II λ 304. An overlapping image in Fe XV λ 284 is at left. Si XI λ 303 is barely separated from He II, as evidenced by a narrow, dark gap between limb brightening in Si XI and the East limb in He II.

A mathematical analogy exists between the inversion of multi-order data and stereoscopy or tomography of an optically thin object. As shown in figure 2, the *object* in (x, λ) space is imaged from several (in this example, three) different "angles". The detector coordinates x' are each different linear combinations of x and λ. In principle, any number of spectral orders may be used; each order provides additional constraints for the interpretation or reconstruction of the object.

We hope that some of the techniques being developed for *MOSES* data analysis will prove useful for the analysis of stereoscopic imaging data that will be obtained by the NASA *STEREO* mission.[7] Indeed, the mathemmatical machinery developed in §§ 4, A is directly applicable to *STEREO* data analysis.

Note that the field of view in (x, λ) space is different for each order (figure 2). Near the ends of the field of view, the sampling of the three detectors is incommensurate; this can only lead to difficulty in reconstructing the object at the left and right edges. This difficulty will be minimized if the instrument bandwidth N_λ is much smaller than the field of view N_x. A narrow passband also simplifies data interpretation, both by the small number of emission lines and by the complete separation of spectral orders in the focal plane. For *MOSES* (§ 5), $N_x/N_\lambda \sim 100$. The *MOSES* passband contains only two detectable emission lines. In contrast, the *Chandra* High Energy Transmission Grating (HETG) is essentially broadband multi-order slitless X-ray spectrograph.[8] Analysis of extended sources with HETG is extremely difficult — and usually limited to forward modeling — in part because of the forest of X-ray lines within the broad instrument passband. Interpretation is further complicated because many orders of the spectrum may overlap on the same detector coordinate.

In short, the information gathered at multiple orders, in a narrow passband, removes much ambiguity from the interpretation of slitless spectrograph data.

3. ANALYSIS TECHNIQUES

This section will outline several ways in which the data from a multi-order, slitless spectrograph may be interpreted. At this point, the description is qualitative. We are actively researching several avenues of data analysis.

3.1. First Steps

Much can be learned by direct inspection of the data. The images from the central order will be immediately useful as pure imaging data, allowing studies of morphology, transverse velocities, etc. Images and movies may be compared directly to data taken by other instruments.

Co-alignment of images from the three detectors may be established in the laboratory by careful metrology and/or end-to-end testing. Cross-correlations among the three orders will serve to confirm the established alignment. Another by-product of cross-correlating the data from multiple orders is that peaks should occur for each spectral line, leading to a first estimate of the aperture-integrated spectrum. The data may then be analyzed more rigorously by a combination of forward modeling and direct inversion techniques.

3.2. Inversion

Given a field of view N_x pixels wide in the dispersion plane, and an instrument wavelength passband spanning N_λ pixels, the slitless spectrograph operating at 3 orders will produce $3N_x$ measured values. But in general, the observed object has $N_x N_\lambda$ degrees of freedom. Thus, we may expect that the forward transform U from the object space to the data space has a null space of dimension $(N_\lambda - 3)N_x$ or greater.

The large nullity makes the inversion appear very difficult, but in fact we know *a priori* that the object space is sparsely filled along the wavelength axis because the object in question is an emission line spectrum. Indeed, the line profiles themselves may be characterized by a small number of parameters. Thus, the solution space has far fewer degrees of freedom than the dimension of (x, λ) space implies. It would seem natural, therefore, to invert the data for line profile parameters. Useful prior constraints for parametric inversion include smoothness of the fitting parameters (in 2 spatial and 1 temporal dimensions); smoothness may be applied locally or by maximizing entropy globally.

3.3. Forward Modeling

The line between direct inversion and forward modeling is fuzzy. We have already mentioned the advantage of putting some physics into the inversion process. Further ground can be gained by testing physical hypotheses against the data by forward modeling. For example, it has been reported that there is an anticorrelation between intensity and linewidth in the He II $\lambda 304$ Å line.[9] Forward modeling of the multi-order data is a straightforward way to discover and study simple relationships of this type.

The overarching difficulty with slitless spectrographs, as with all ill-posed problems, is the non-uniqueness of solutions. We argued in § 3.2 that the dimension of the nullspace (in the (x, λ) representation) is not necessarily a measure of the ambiguity in interpreting the data. Rather, we should ask: "to what extent does the null space cause confusion between physically meaningful interpretations?". As a first step in this direction, the next section will characterize the null space of a theoretically ideal instrument.

4. CHARACTERIZATION OF THE INSTRUMENTAL NULL SPACE

In order to understand the advantages and limitations of multi-order instruments generally, and *MOSES* in particular, we would like to map out the "null space" of objects for which the *ideal* instrument response is zero. The integral equations describing an ideal three-order slitless spectrograph are given in § 4.1. In § 4.2, we derive a straightforward description of the null space for an ideal instrument in terms of a differential operator acting on an arbitrary generating function. The utility of this representation will become apparent when it is applied to a system with a discrete (pixellated) detector (§4.3). Finally in §4.4, we show a few practical implications for data interpretation, instrument design, and observing strategy.

Much work is yet to be done. The description of the null space (strictly defined, as in this section) does not address the set of objects for which the instrument response is nonzero, but small compared to noise. This significant project is left for the future.

4.1. Ideal Three-Order Instrument

A three-order, narrowband, slitless spectrograph transforms an object $v(x, \lambda)$ into three overlappograms. We will call the set of three overlappograms $\mathbf{I} = (I_+(x+\lambda), I_0(x), I_-(x-\lambda))$, where x and λ are measured in pixels. A measurement made by an ideal instrument may be described as a linear transform U,

$$\mathbf{I} = Uv. \tag{1}$$

The operator U integrates along three camera angles, as illustrated in figure 2. The resulting images are:

$$\begin{aligned}
I_0(x') &= \int_{\lambda=\lambda_0-\Delta}^{\lambda_0+\Delta} v(x,\lambda)\, d\lambda, \quad (x = x'); \\
I_-(x') &= \int_{\lambda=\lambda_0-\Delta}^{\lambda_0+\Delta} v(x'+\lambda-\lambda_0,\lambda)\, d\lambda = \int_{\substack{x=x'-\Delta \\ \lambda=\lambda_0-\Delta}}^{\substack{x'+\Delta \\ \lambda_0+\Delta}} v(x,\lambda)\, d(\lambda+x); \\
I_+(x') &= \int_{\lambda=\lambda_0-\Delta}^{\lambda_0+\Delta} v(x'-\lambda+\lambda_0,\lambda)\, d\lambda = \int_{\substack{x=x'+\Delta \\ \lambda=\lambda_0-\Delta}}^{\substack{x'-\Delta \\ \lambda_0+\Delta}} v(x,\lambda)\, d(\lambda-x);
\end{aligned} \tag{2}$$

where x' is the coordinate on the detector, λ_0 is the central wavelength of the instrument passband, and Δ is the half-width of the instrument passband. The integrals along the diagonals we have rewritten in a notation that is intended to emphasize the direction of integration, using variables $\lambda + x$ and $\lambda - x$. We will ignore the "edge effects" due to finite field of view in x'.

4.2. Null Space

The true object $v(x, \lambda)$ observed by the slitless spectrograph is not a unique solution of equation (1). Consider an alternative solution $v' \neq v$. Since U is linear,

$$Uv' - Uv = U(v' - v) = 0$$

For any alternative solutions v and v', there exixts a *null* $f = v' - v$. The null space of the forward transform U is the set of objects $f(x, \lambda)$ that satisfy

$$Uf = 0.$$

The nullspace embodies all of the possible ambiguity in interpreting the data. In terms of equations (2), a null function f must satisfy

$$\int_{\lambda=\lambda_0-\Delta}^{\lambda_0+\Delta} f(x,\lambda)\,d\lambda = \int_{\substack{x=x'-\Delta\\ \lambda=\lambda_0-\Delta}}^{\substack{x'+\Delta\\ \lambda_0+\Delta}} f(x,\lambda)\,d(\lambda+x) = \int_{\substack{x=x'+\Delta\\ \lambda=\lambda_0-\Delta}}^{\substack{x'-\Delta\\ \lambda_0+\Delta}} f(x,\lambda)\,d(\lambda-x) = 0. \tag{3}$$

Motivated by the integral equations, we define the generating function

$$g(x,\lambda) = \int\int\int f\,d\lambda\,d(\lambda+x)\,d(\lambda-x), \quad \text{or} \tag{4}$$

$$\begin{aligned} f(x,\lambda) &= \frac{\partial}{\partial\lambda}\,\frac{\partial}{\partial(\lambda+x)}\,\frac{\partial}{\partial(\lambda-x)}\,g(x,\lambda), \\ &= \frac{\partial}{\partial\lambda}\left(\frac{\partial}{\partial\lambda}+\frac{\partial}{\partial x}\right)\left(\frac{\partial}{\partial\lambda}-\frac{\partial}{\partial x}\right)g(x,\lambda). \end{aligned} \tag{5}$$

Now we ask, what are the necessary and sufficient conditions on choosing g so that f is a null? It turns out that we may adopt the simple criteria that g and its first and second derivatives are zero at $\lambda=\lambda_0-\Delta$, and the second derivatives of g are zero at $\lambda=\lambda_0+\Delta$. Under this set of assumptions, there is a 1:1 mapping between the set of all possible generating functions g and the set of all possible nulls f. Under certain conditions, we may adopt an even simpler rule that g and its derivatives are zero at both the upper and lower boundaries in λ. The demonstration of this is left for the Appendix (§A).

4.3. Discrete Representation

We now consider an instrument with discrete pixels. The object to be observed, v_{ij}, is a grid of pixels indexed by position i and wavelength j. We will discretize the integral equations (2) as follows.

$$\begin{aligned} I_i^0 &= \sum_{i=0}^{N_\lambda} v_{ij}, \\ I_i^- &= \sum_{i=0}^{N_\lambda} v_{i+j-\Delta,j}, \\ I_i^+ &= \sum_{i=0}^{N_\lambda} v_{i-j+\Delta,j}, \end{aligned} \tag{6}$$

where the number of wavelength pixels in the passband is $N_\lambda = 2\Delta$.This defines the instrument operator U in the discrete representation. The index i is the detector coordinate for each overlappogram.

In the previous section, we described an element f of the instrumental null space as a third derivative of a generating function: $f = \partial_\lambda\,\partial_{\lambda+x}\,\partial_{\lambda-x}\,g$. Differential operators in continuous space may be represented as convolutions in discrete space. The equivalences below relate differential operators to convolution kernels.

$$\begin{aligned} \frac{\partial}{\partial\lambda} &\longleftrightarrow \begin{pmatrix} 1 \\ -1 \end{pmatrix}. \\ \frac{\partial}{\partial(\lambda+x)} &\longleftrightarrow \begin{pmatrix} 0 & 1 \\ -1 & 0 \end{pmatrix}. \\ \frac{\partial}{\partial(\lambda-x)} &\longleftrightarrow \begin{pmatrix} 1 & 0 \\ 0 & -1 \end{pmatrix}. \\ \frac{\partial}{\partial\lambda}\,\frac{\partial}{\partial(\lambda+x)}\,\frac{\partial}{\partial(\lambda-x)} &\longleftrightarrow \kappa \equiv \begin{pmatrix} 0 & -1 & 0 \\ 1 & 1 & 1 \\ -1 & -1 & -1 \\ 0 & 1 & 0 \end{pmatrix}. \end{aligned} \tag{7}$$

The final result (7) is obtained by successive convolution of the kernels used to represent ∂_λ, $\partial_{\lambda+x}$, and $\partial_{\lambda-x}$. Every null $f_{x,\lambda}$ in the discrete space may be represented as a convolution of the kernel in (7) with a generating function g_{ij}:

$$f = \kappa \otimes g. \tag{8}$$

The null space therefore consists of superpositions of the 3×4 kernel κ.

4.4. Implications

Fortunately, the addition of an arbitrary null f to the true solution v often results in an absurd solution that does not resemble an EUV emisson line spectrum. There is reason for concern only when the solutions v and $v + f$ appear equally plausible from a physical standpoint. The ambiguity between them is then impossible to resolve. We are therefore motivated to discover nulls f that resemble differences between physically believable solutions.

This subsection provides two simple examples of the physical ambiguity generated by the null space. In each case, strategies are suggested to mitigate the ambiguity.

4.4.1. Sensitivity to Local Variations in the Line Profile

In wavelength λ, the null κ derived above has zero first and second moments, but a nonzero third moment. Since κ is very compact, its addition to the true solution v may result in virtually arbitrary, local variations in the third moment of the line profile. The three-order spectrograph is therefore relatively insensitive to line asymmetry (and higher moments) of the line profile. This conclusion might have been anticipated on the grounds that the data contain three pieces of information (I_0, I_+, I_-) for each image pixel. These three degrees of freedom correspond roughly to the line intensity, doppler shift, and line width as a function of position.

Any strategy for data inversion or forward modeling should take into account the limitations of the instrument configuration. The proper approach is to include only as many parameters as are needed to fit the data to within measurement error. If measurements of the higher moments of the line profile are desired, it is possible (at least in principle) to derive them from images obtained at higher orders such as $n = \pm 2$.

4.4.2. Sensitivity to Nonlocal variations in the Line Profile

We now introduce an especially pernicious class of nulls that have some capacity to influence the apparent line intensities, doppler shifts, and line widths observed with a three-order slitless spectrograph. Ambiguity in the lower moments of the line profile is possible only with nulls that extend across the entire field of view in the dispersion plane. We will give an example of such a null, and then describe the means to eliminate these "nonlocal" nulls by a combination of instrument design and observational strategies.

Figure 4 illustrates a null that we call the "periodic bipole". The periodic bipole consists of two rows of dots, one positive and one negative, equally spaced in x and λ so as to cancel from all three points of view. Since the solution space $(x, lambda)$ is sparsely filled with emission lines, most possible placements of the null will violate non-negativity. However, if the position and spacing of these rows in λ coincides with two observed emission lines, then the null effectively subtracts intensity from one line and adds it to another.

There is another pernicious aspect to the periodic bipole. We expect the ambiguity of measurement (and the instrumental null space) to diminish if detectors are added to the instrument at more spectral orders. However, the periodic bipole remains an element of the nullspace no matter how many orders are imaged by the insrument. That is, sums along lines of constant $x \pm n\lambda$ yield zero results for all integers n.

Fortunately, the ambiguities caused by the periodic bipole can be minimized or even eliminated. Since the amplitude of this null does not vary as a function of x, it is likely that one of the negative pixels in f will fall on a pixel within v that is small or zero. Thus, the non-negativity constraint comes to our aid. We may take better advantage of non-negativity by adjusting our observing strategy to include a dim region (e.g. above the solar limb). Alternatively, a permanent dark region may be built into the instrument by adding a field stop to the optical system (at the cost of re-imaging before the dispersive element). This is an application of the principle derived in §A.2: a region of zero (or low) intensity in the image, combined with the non-negativity

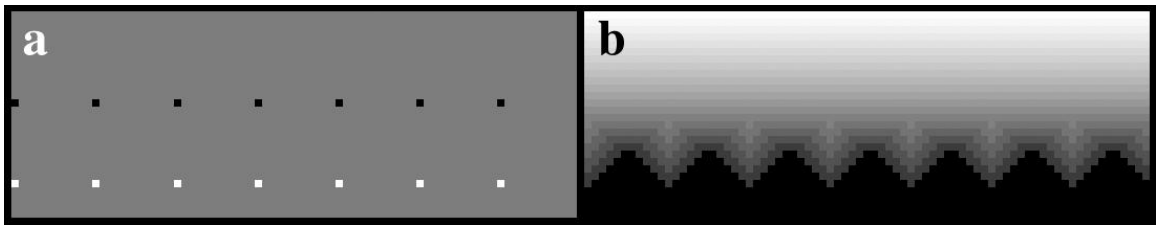

Figure 4. (a) A null pattern composed of two rows of dots, one positive and one negative (gray repesents zero). The space between the rows equals the horizontal spacing of the dots. (b) The generating function g for this null, square root scaled to enhance contrast of dim features.

constraint, will prevent (or minimize) the contamination of the true solution with nulls that are nonlocal. A nonlocal null may be defined operationally as one whose generating function g does not satisfy the stronger form of the boundary conditions derived in the Appendix (equations 15).

5. THE *MOSES* SOUNDING ROCKET PAYLOAD

A proof of concept sounding rocket payload, the *Multi-Order Solar EUV Spectrograph* (*MOSES*), is under development by an international collaboration including Montana State University (MSU), Goddard Space Flight Center (GSFC), Lockheed-Martin Solar & Astrophysics Laboratory (LMSAL), and Mullard Space Sciences Laboratory (MSSL). *MOSES* is a three year program funded by the NASA Low Cost Access to Space (LCAS) program. *MOSES* will demonstrate narrowband, multi-order imaging and spectroscopy of the solar chromosphere and corona.

5.1. Science Objectives

The *MOSES* payload will examine the formation of the He II λ303.8 Åline, which is anomalously bright compared to other lines that are believed to form at the same temperatures.[10] For the first time, doppler and linewidth maps will be obtained at high cadence in EUV. Variations in line width, line intensity, and doppler shift of the He II resonance line will be studied to elucidate the line formation mechanism. The Si XI λ303.3 line, also in the *MOSES* passband, will provide data on the relationship between coronal and chromospheric features, shedding light on the interface between these two very different layers of the solar atmosphere. Coronal intensities will also be of help in searching for any signature of He II excitation by photoionization and recombination.

5.2. Instrument Characteristics

The optical characteristics described here are the proposed baseline; a final, optimized design will be reported in the near future. *MOSES* is a $f/62$ objective grating spectrograph operating at λ 293-314 Å in orders $n = -1, 0, +1$. In the outboard orders, each pixel subtends 21 mÅ.

The primary mirror is a 10.8 m spherical grating, ruled at 1160 lines/mm. A flat secondary mirror folds the optical path approximately in half. Ray traces show that spatial resolution in the central order is pixel limited at $1''$. The spatial and spectral resolution in the outboard orders is limited by aberration, with an RMS spot radius of $0\farcs62$. Aberrations contribute 56 mÅto the measured linewidth.

EUV reflectivity at 304 Åis maximized, and off-band sensitivity minimized, by Ir/Si multilayer coatings on both reflecting elements. Visible light is rejected by thin film filters placed between the folding flat and the detectors. The signal in the three orders is approximately equalized by using more and/or thicker filters in the central diffraction order.

The detectors are three Marconi 42-20 (or 42-10) 2048×1024 (512) thinned, back-illuminated CCDs, with a quantum efficiency of $\sim 80\,\%$ @ 600 Å. The resulting field of vew is $17'$ wide in the dispersion plane, and $8\farcm5$ ($4\farcm3$) high.

Based on the average active region spectrum gathered by SERTS-95,[11] The mean predicted signal level for *MOSES* is $\sim$ 600 counts per pixel in a 1 s exposure, per order ($n = \pm 1$). The three strongest contributions are from lines of He II λ303.8 (89 %), Si XI λ303.3 (8 %) and Fe XV λ284.2 (2 %). An active region target is desirable to maximize contrast. If no active region is visible at the time of launch, quiet sun exposures will be of order 10 s. With readout times of ~ 2 s, *MOSES* will be capable of $3 - 12$ s cadence.

6. CONCLUSIONS

A narrowband slitless spectrograph operating in multiple diffraction orders. This approach allows high speed imaging spectroscopy of just a few emission lines.

The limitations of a three-order design have been explored in a preliminary way by deriving an exact representation of the instrumental null space— that set of functions f that produce no response, leading to ambiguity in data interpretation. We conclude that an instrument of three-order design is insensitive to the third and higher moments of the line profile. More analysis is required to characterize the instrument sensitivity to line ratios, doppler shifts, and line width in the presence of noise. However, at this stage it is apparent that large contrasts (in particular, the presence within the field of view of areas of low intensity) will help to minimize the ambiguity in the data. It is possible to assure the presence of appropriate contrasts by observing strategy or by designing an instrument that images onto a focal plane with a field stop upstream from the dispersive element.

Interestingly, the mathematical machinery used here for describing the null space of a multi-order slitless spectrograph is well suited to describing the nullspace of the STEREO instrument. That nullspace will be larger because only two points of view are involved, rather than three.

The *MOSES* rocket payload, now funded by the NASA LCAS program, will be the first demonstration of narrowband, slitless spectrometry. The first launch of *MOSES*, in Spring of 2004, will facilitate a new understanding of the solar chromosphere and corona. For the first time, high cadence maps of linewidth and doppler shift will be obtained in an EUV spectral line. *MOSES* will simultaneously image He II and Si XI at 1″ resolution, map line of sight motions in the chromosphere to $\sim$ 20 km/s, and search for nonthermal line broadening. This will provide critical tests of theories that have been advanced for the formation of the chromospheric He II λ 304 resonance line.

APPENDIX A. THE GENERATING FUNCTION

In §4.2, the question arose: what conditions on the generating function g are necessary and sufficient so that f is an element of the nullspace of U? We may obtain an answer directly by rewriting equation (3) in terms of g:

$$\begin{aligned}
\left[\left(\frac{\partial}{\partial\lambda}+\frac{\partial}{\partial x}\right)\left(\frac{\partial}{\partial\lambda}-\frac{\partial}{\partial x}\right)g\right]_{\lambda=\lambda_0-\Delta}^{\lambda=\lambda_0+\Delta} &= 0,\\
\left[\frac{\partial}{\partial\lambda}\left(\frac{\partial}{\partial\lambda}-\frac{\partial}{\partial x}\right)g\right]_{\substack{x=x'-\Delta\\ \lambda=\lambda_0-\Delta}}^{\substack{x'+\Delta\\ \lambda_0+\Delta}} &= 0, \qquad (9)\\
\left[\frac{\partial}{\partial\lambda}\left(\frac{\partial}{\partial\lambda}+\frac{\partial}{\partial x}\right)g\right]_{\substack{x=x'+\Delta\\ \lambda=\lambda_0-\Delta}}^{\substack{x'-\Delta\\ \lambda_0+\Delta}} &= 0.
\end{aligned}$$

This result is rather unsatisfactory. It is difficult to understand intuitively what sort of function g would satisfy the above expressions. Moreover, we see no straightforward way to use these constraints to construct arbitrary generating functions g. These shortcomings will be put to rest in § A.1 by carefully choosing constants of integration for deriving g from f. Then, in § A.2, we will find a way to pare down the nullspace, resulting in the simplified constraint that g and its derivatives are zero at $\lambda = \lambda_0 \pm \Delta$.

A.1. Boundary Conditions on g

The null function f is expected to approach zero at the boundaries because of the instrument passband filter. At the lower boundary, for example,

$$f(x,\lambda) = 0, \quad \lambda < \lambda_0 - \Delta. \tag{10}$$

Since the triple integral of equation (4) is indefinite, we are free to begin integrating at the lower boundary, where we may choose the boundary condition

$$g(x, \lambda_0 - \Delta) = 0. \tag{11}$$

Because of the boundary condition on f (equation 10), the derivatives of g at the lower boundary are also zero:

$$\frac{\partial g}{\partial \lambda} = \frac{\partial g}{\partial x} = \frac{\partial^2 g}{\partial x^2} = \frac{\partial^2 g}{\partial \lambda^2} = \frac{\partial^2 g}{\partial x \partial \lambda} = 0, \quad \lambda = \lambda_0 - \Delta \tag{12}$$

Thse lower boundary conditions result from exercising a kind of "gauge" freedom, equivalent to an arbitrary choice of the constants of integration for the generating function g. Within the chosen gauge, g is uniquely determined for a given f. For this choice of gauge, equations 9 are easily solved for the upper wavelength boundary. The result is that the second derivatives of g are zero along the top boundary:

$$\frac{\partial^2 g}{\partial x^2} = \frac{\partial^2 g}{\partial \lambda^2} = \frac{\partial^2 g}{\partial x \partial \lambda} = 0, \quad \lambda > \lambda_0 + \Delta \tag{13}$$

That is, the generating function becomes a plane at the top boundary: $g(\lambda, x) = a\lambda + bx + c$. By deriving this from equations (9), we have shown that equations (12 - 13) are sufficient to guarantee that $f = \partial_\lambda \partial_{\lambda+x} \partial_{\lambda-x} g$ is an element of the nullspace of U. Likewise, a unique g satisfying equations (12 - 13) may be constructed for any null object f.

A.2. More Restrictive Boundary Conditions on g

It is possible to make the boundary conditions on g more restrictive, reducing the size of the null space. Suppose that the null f is zero over some interval in x. This interval could occur at the left or right edge of the domain, or somewhere in the middle.

$$f(x,\lambda) = 0, \quad x_0 \le x \le x_1. \tag{14}$$

If $x_1 - x_0 > 4\Delta$, then when g is calculated by integrating from the bottom, we will find that $g = 0$ over some finite interval along the top boundary. If we then apply the uppper boundary condition (13), it follows that

$$\frac{\partial g}{\partial \lambda} = \frac{\partial g}{\partial x} = \frac{\partial^2 g}{\partial x^2} = \frac{\partial^2 g}{\partial \lambda^2} = \frac{\partial^2 g}{\partial x \partial \lambda} = 0, \quad \lambda = \lambda_0 + \Delta. \tag{15}$$

There are several practical ways to impose the added boundary condition (14):

- observe an object that has finite extent, such as the solar limb or a bright active region;
- include a dark patch, such as a coronal hole in the field of view;
- employ a field stop in the optical system.

In either case, the object $v(x,\lambda)$ is zero (or at least very small) over the interval $[x_0, x_1]$. Nulls not satisfying the more restrictive boundary condition cannot be added to the true solution v, because it would violate the non-negativity constraint. The result is that the generating function for nulls, g, and its derivatives, must be zero along (at least) the upper and lower boundaries in λ. Some particularly insidious null functions may be excluded by these means (§ 4.4.2).

ACKNOWLEDGMENTS

The MOSES sounding rocket project is supported by NASA grant NAG5-10997. CCK would like to thank Dr Dana Longcope of Montana State University for many stimulating and helpful discussions.

REFERENCES

1. B. N. Handy, L. W. Acton, C. C. Kankelborg, C. J. Wolfson, D. J. Akin, M. E. Bruner, R. Caravalho, R. C. Catura, R. Chevalier, D. W. Duncan, C. G. Edwards, C. N. Feinstein, S. L. Freeland, F. M. Friedlaender, C. H. Hoffmann, N. E. Hurlburt, B. K. Jurcevich, N. L. Katz, G. A. Kelly, J. R. Lemen, M. Levay, R. W. Lindgren, D. P. Mathur, S. B. Meyer, S. J. Morrison, M. D. Morrison, R. W. Nightingale, T. P. Pope, R. A. Rehse, C. J. Schrijver, R. A. Shine, L. Shing, K. T. Strong, T. D. Tarbell, A. M. Title, D. D. Torgerson, L. Golub, J. A. Bookbinder, D. Caldwell, P. N. Cheimets, W. N. Davis, E. E. Deluca, R. A. McMullen, H. P. Warren, D. Amato, R. Fisher, H. Maldonado, and C. Parkinson, "The transition region and coronal explorer," *Sol. Phys.* **187**, pp. 229–260, July 1999.
2. C. J. Schrijver, A. M. Title, T. E. Berger, L. Fletcher, N. E. Hurlburt, R. W. Nightingale, R. A. Shine, T. D. Tarbell, J. Wolfson, L. Golub, J. A. Bookbinder, E. E. Deluca, R. A. McMullen, H. P. Warren, C. C. Kankelborg, B. N. Handy, and B. de Pontieu, "A new view of the solar outer atmosphere by the transition region and coronal explorer," *Sol. Phys.* **187**, pp. 261–302, July 1999.
3. J. T. Mariska, C. M. Brown, K. P. Dere, G. A. Doschek, C. M. Korendyke, J. L. Culhane, and T. Watanabe, "The Extreme Ultraviolet Imaging Spectrometer on Solar-B," in *American Geophysical Union, Spring Meeting 2001, abstract #SH41A-12*, pp. 41A12+, May 2001.
4. B. J. Kent, R. A. Harrison, E. C. Sawyer, R. W. Hayes, A. G. Richards, J. L. Culhane, K. Norman, A. A. Breeveld, P. D. Thomas, A. I. Poland, R. J. Thomas, W. T. Thompson, B. R. Aschenbach, H. W. Braeuninger, O. Kjeldseth-Moe, M. Kuehne, J. Hollandt, W. Paustian, and B. J. Bromage, "Coronal Diagnostic Spectrometer: an extreme-ultraviolet spectrometer for the Solar and Heliospheric Observatory," in *Proc. SPIE Vol. 2517, p. 12-28, X-Ray and EUV/FUV Spectroscopy and Polarimetry, Silvano Fineschi; Ed.*, vol. 2517, pp. 12–28, Oct. 1995.
5. K. Wilhelm, W. Curdt, E. Marsh, U. H. Schuehle, P. Lemaire, A. H. Gabriel, J.-C. Vial, M. Grewing, M. C. Huber, S. D. Jordan, A. I. Poland, R. J. Thomas, M. Kuehne, J. G. Timothy, D. M. Hassler, and O. H. Siegmund, "Some design and performance features of SUMER: solar ultraviolet measurements of emitted radiation," in *Proc. SPIE Vol. 2517, p. 2-11, X-Ray and EUV/FUV Spectroscopy and Polarimetry, Silvano Fineschi; Ed.*, vol. 2517, pp. 2–11, Oct. 1995.
6. R. Tousey, J. . F. Bartoe, G. E. Brueckner, and J. D. Purcell, "Extreme ultraviolet spectroheliograph atm experiment s082a," *Appl. Opt.* **16**, pp. 870–878, Apr. 1977.
7. J. M. Davila, D. M. Rust, V. J. Pizzo, and P. C. Liewer, "Solar Terrestrial Relations Observatory (STEREO)," in *Proc. SPIE Vol. 2804, p. 34-38, Missions to the Sun, David M. Rust; Ed.*, vol. 2804, pp. 34–38, Nov. 1996.
8. A. C. Brinkman, "The advanced x-ray astrophysics facility," *Advances in Space Research* **11**, pp. 231–241, 1991.
9. V. Andretta, S. D. Jordan, J. W. Brosius, J. M. Davila, R. J. Thomas, W. E. Behring, W. T. Thompson, and A. Garcia, "The role of velocity redistribution in enhancing the intensity of the he ii 304 å line in the quiet-sun spectrum," *ApJ* **535**, pp. 438–453, May 2000.
10. V. Andretta and H. P. Jones, "On the role of the solar corona and transition region in the excitation of the spectrum of neutral helium," *ApJ* **489**, pp. 375+, Nov. 1997.
11. J. W. Brosius, J. M. Davila, and R. J. Thomas, "Solar active region and quiet-sun extreme-ultraviolet spectra from serts-95," *ApJS* **119**, pp. 255–276, Dec. 1998.